

Beam commissioning of the 35 MeV section in an intensity modulated proton linear accelerator for proton therapy

L. Picardi,¹ A. Ampollini,¹ G. Bazzano,¹ E. Cisbani,² F. Ghio,² R. M. Montereali,¹
 P. Nenzi,¹ M. Piccinini,¹ C. Ronsivalle,^{1,*} F. Santavenere,² V. Surrenti,¹ E. Trinca,¹
 M. Vadrucchi,¹ and E. Wembe Tafo³

¹ENEA, Via Enrico Fermi 45, 00044 Frascati, Rome, Italy

²Italian Institute of Health (ISS), Viale Regina Elena 299, 00161 Rome, Italy

³University of Douala, Carrefour Ange Raphaël, Douala, Cameroon



(Received 1 March 2019; accepted 21 January 2020; published 26 February 2020)

This paper presents the experimental results on the Terapia Oncologica con Protoni-Intensity Modulated Proton Linear Accelerator (TOP-IMPLART) beam that is currently accelerated up to 35 MeV, with a final target of 150 MeV. The TOP-IMPLART project, funded by the Innovation Department of Regione Lazio (Italy), is led by Italian National Agency for New Technologies, Energy and Sustainable Economic Development (ENEA) in collaboration with the Italian Institute of Health and the Oncological Hospital Regina Elena-IFO. The accelerator, under construction and test at ENEA-Frascati laboratories, employs a commercial 425 MHz, 7 MeV injector followed by a sequence of 3 GHz accelerating modules consisting of side coupled drift tube linac (SCDTL) structures up to 71 MeV and coupled cavity linac structures for higher energies. The section from 7 to 35 MeV, consisting on four SCDTL modules, is powered by a single 10 MW klystron and has been successfully commissioned. This result demonstrates the feasibility of a “fully linear” proton therapy accelerator operating at a high frequency and paves the way to a new class of machines in the field of cancer treatment.

DOI: [10.1103/PhysRevAccelBeams.23.020102](https://doi.org/10.1103/PhysRevAccelBeams.23.020102)

I. INTRODUCTION

Radiation therapy is one of the cornerstones of cancer treatment. The exposure of tumor tissues to ionizing radiation induces unrecoverable damage to DNA of the cancerous cells, leading to their death. Photons and heavy charged particles (hadrons) are the most used radiation sources. X rays, in particular, represent the most widespread choice, since they can be easily produced from compact and cost-effective electron accelerators. Photons, however, lose their energy in matter as a function of the penetration depth in an exponentially decreasing fashion. This implies that the target has to be irradiated from multiple directions, in order to reduce the dose released to surrounding healthy tissues while keeping constant the one delivered to the tumor. In this regard, hadrons present some advantages over x rays. The energy deposition curve exhibits a small amount of energy lost when the particle velocity is high (entry channel), while most of it is lost in a narrow portion of the path, the so-called Bragg peak, close

to the end of the particle range. Moreover, hadron beams are characterized by a lower lateral scattering with respect to x rays, resulting in a more conformal irradiation of the tumor volume.

Despite the recognized therapeutic benefit, the complexity, dimensions, and costs (e.g., construction operation and maintenance) of the facility have hindered a large-scale diffusion of particle therapy centers, until progress in accelerator technologies and treatment plan implementation has changed course. Nowadays, there are 87 particle therapy facilities worldwide, 11 of which use also carbon ions [1], and they all rely on circular machines to accelerate particles. The majority of proton facilities use a cyclotron as an accelerator, while proton-carbon ones employ a synchrotron. It is generally acknowledged, however, that more compact and efficient accelerators must be developed to reduce treatment duration (hypofractionation), improve dose delivery precision, and reduce costs, with the aim to make proton facilities more profitable, thus closing the gap with x-ray machines.

At the beginning of the 1990s [2,3], high-frequency pulsed linear accelerators were proposed as a possible compact, lightweight, and cost-effective solution for proton therapy thanks to the small dimensions of the accelerating structures and to the use of commercially available rf power sources. In a comprehensive study, reported in Ref. [4], two

*concetta.ronsivalle@enea.it

different approaches were suggested: a hybrid cyclotron linac (the so-called Cyclinac, supported by Amaldi *et al.* [5,6]) and a fully linear accelerator. The former consisted of a 62.5 MeV cyclotron injector feeding an L-band (1.28 GHz) linac booster, reaching a final energy of 200 MeV. The second one, instead, exploited a typical sequence of accelerating structures for proton linacs: a proton source; a UHF (499.5 MHz) radio frequency quadrupole (RFQ) preaccelerator; a drift tube linac (DTL) operating at the same frequency (up to an energy around 70 MeV); and a sequence of coupled cavity linacs (CCLs), operating in the microwave S band (2.997 GHz), to a final energy between 230 and 250 MeV. Following this approach, in 1995, Ente Nazionale Energie Alternative (ENEA) patented a 200 MeV fully linear compact proton accelerator [7]. It employed a novel and lightweight S-band accelerating structure named side coupled drift tube linac (SCDTL) to be used for particle energies between 5 and 65 MeV.

In 2012, the Innovation Department of Regione Lazio funded a project named Terapia Oncologica con Protoni-Intensity Modulated Proton Linear Accelerator for Radio Therapy (TOP-IMPLART) [8], aiming to realize and validate a prototype of a linear accelerator, built with SCDTL technology, dedicated to proton therapy. The accelerator is under development at the ENEA research center in Frascati, in collaboration with the Italian Institute of Health, and the Oncological Hospital IFO. Following the criteria presented in the original patent, in the actual design, SCDTL modules constitute the accelerating sections between 7 and 71 MeV.

The use of high-frequency proton linacs has several advantages over circular machines. For instance, the output charge rate can be flexibly varied by either changing the injector current, shortening the current pulse duration, or changing the optics parameters in the injection line. Output energy can be varied by switching off some of the modules and adjusting the rf power level in the last one [4,8]. Thus, intensity and energy could be changed ideally at each pulse (i.e., every 5–10 ms), resulting in a fast and effective modulation of the output beam. In clinical practice, this allows one to move from one tumor slice to the next much faster than the several hundreds of milliseconds needed by circular machines, provided that the magnetic elements of the transport line and gantry are able to react at the same velocity. Moreover, linear accelerators can achieve very low beam emittance (rms normalized 0.2π mm-mrad in TOP-IMPLART, or even better with a lower emittance injector). This allows smaller apertures for magnets and considerably reduces the weight of the gantry [4]. As far as radiation protection is concerned, the use of linear accelerators is less demanding, since the radiation losses occur at a low energy [9].

The TOP-IMPLART project foresees a proton final energy of 150 MeV (phase 1, funded with 11 M€), limited by the maximum bunker length available (30 m) at the

Frascati site (where clinical experimentation is not allowed), with the possibility to upgrade the machine to 230 MeV directly in the hosting medical center (phase 2). Nevertheless, the 150 MeV proton beam has a sufficient penetration depth to treat at least half of all lesions eligible for proton therapy (including ocular melanoma and head-neck and pediatric tumors) [8].

The excellent perspectives of a proton therapy dedicated linac, and the promising results of SCDTL structures, encouraged the growth of two industrial initiatives, Linac for Image Guided Hadron Therapy (LIGHT) and Enhanced Radioterapy with HAdrons (ERHA) [10–13], to develop a commercial proton therapy linear accelerator. Both projects started before the definitive experimental demonstration of the SCDTL concept, which occurred in 2014 at the TOP-IMPLART facility [14]. Based on detailed studies provided by ENEA, both LIGHT and ERHA employ SCDTL sections after the injector, up to energies of about 30 MeV. Further acceleration, in both projects, is obtained with CCL sections. This design choice favors the accelerator compactness (in comparison to TOP-IMPLART that employs SCDTLs up to 71 MeV), as CCLs have a higher accelerating gradient, at the expense of the rf power required for acceleration. The TOP-IMPLART design, instead, focuses on optimizing the machine stability by reducing the number of rf power units, especially in the midenergy range. The consequent accelerator lengthening has been considered of secondary importance, if compared to the higher cost, management, and spare parts procurement that would be needed for the rf power increase.

Thus, the successful commissioning of four SCDTL modules from 7 to 35 MeV, powered by a single 10 MW klystron, has a crucial importance for all the aforementioned proton therapy linacs. In fact, it constitutes the demonstration that this type of structures can be employed as building blocks of a high-frequency linear accelerator for cancer therapy applications.

Furthermore, machine development in terms of energy upgrade, stability, and repeatability has been complemented by dosimetry and radiobiology experiments that validate the quality of the beam. This approach presents several benefits: It allows testing and calibrating specific instrumentation for pulsed beams (large instantaneous dose rate even at a low average dose rate) and enables evaluation of the biological effects of the beam.

The paper is organized as follows: Sec. II gives an overview of the main characteristics of the TOP-IMPLART accelerator; Sec. III describes in detail the operation of the four SCDTL modules at 35 MeV and the relative diagnostics. Finally, Sec. IV reports the experimental results concerning the beam characterization at two different positions: at the linac exit window and in air at a distance of 1.8 m, where the beam is used for radiobiological “in vitro” and “in vivo” experiments. The paper ends with future plans and final considerations.

II. THE TOP-IMPLART LINAC

A. Accelerator layout

The TOP-IMPLART linac consists of a 7 MeV commercial injector (Duoplasmatron source, RFQ, and DTL) produced by ACCSYS-Hitachi (PL7 model) operating at 425 MHz [15] and a high-frequency linear accelerator operating at 2997.92 MHz completely designed by ENEA. This latter segment is composed by SCDTL structures up to 71 MeV and CCL structures up to 150 MeV. A medium energy beam transport line (MEBT) with four electromagnetic quadrupoles is placed between the injector and the first SCDTL module; it also includes a 90° bending magnet that can deflect the beam into a short vertical beam line dedicated to radiobiology experiments. A schematic layout of the TOP-IMPLART linac is shown in Fig. 1. The high-frequency part consists of four sections, each powered by a 10 MW klystron.

The main design parameters of the high-frequency linac are summarized in Table I.

The accelerator rf system operates in pulsed mode. The pulse length is 15–80 μ s for the injector and 1–4 μ s for the high-frequency linac. The maximum repetition frequency is currently designed to be 100 Hz, mainly due to the limits of the injector currently in use. A single FPGA-based timing unit synchronizes injector and booster operation, generating a set of triggers with a jitter below 10 ns.

The availability of off-the-shelf proton injectors working at 425 MHz and of standard European S-band (2998.5 MHz) klystrons and rf components already procured in the past led to a rf frequency for the injector that is not a subharmonic of the SCDTL or CCL one. This implies that there is no longitudinal matching between low- and high-frequency modules, leading to large particle losses at 7 MeV in the first SCDTL module.

Nevertheless, the injected current is sufficiently high to produce an output current much larger than what is actually required for proton therapy. Moreover, the beam losses raise no particular concern as to radiation protection limits, since they all occur at a low proton energy.

This unconventional and somewhat inefficient modality will likely be reconsidered in the future, i.e., when the TOP-IMPLART system is engineered and moved to a

hospital environment. Currently, there are two options under review. The first foresees the acquisition of a synchronous injector with a lower output energy (as in LIGHT and ERHA machines) and the addition of a SCDTL module before SCDTLA. The second option keeps the actual PL7 injector, adding two cavities, one debuncher, and one buncher, as presented in Ref. [16]. In both cases, the bending magnet will be eliminated from the layout, as it not necessary for the clinical application.

The rf power distribution system is able to produce energy variation between 71 and 150 MeV, needed to perform a distal to proximal scan of the tumor volume. It is obtained by progressively switching off high-energy modules in the last two accelerating sections (referred to as 3 and 4 in Table I) and varying the electric field amplitude in the last accelerating module from 0 to 100% [9]. The energy gain of those modules has been optimized through beam dynamics simulations, to obtain a good quality beam at any power level.

Variable rf power dividers regulate the rf level of the last two klystrons with a dedicated control system. The rf power of sections 3 and 4 can be completely diverted to a matched load to switch off the last modules. Phase shifters before each module will provide proper rf field phasing.

B. The SCDTL structure

The SCDTL structure [16–20] was invented to compact UHF-DTL structures typically used in proton linear accelerator medium-energy sections with the aim to make them work at frequencies as high as 3 GHz. The corresponding reduction of the structure axial hole for beam transport, from centimeter size to millimeter size, is compatible with the very low currents required by proton therapy.

Obviously, the reduction in size of the drift tubes prevents the accommodation of the permanent magnet quadrupoles (PMQs) inside them. The accelerating action of the DTL tanks has therefore been spatially separated from the focusing action by splitting DTL tanks in smaller units and placing PMQs in the intratank space. The tanks are rf coupled together by side coupling cavities, explaining the name SCDTL.

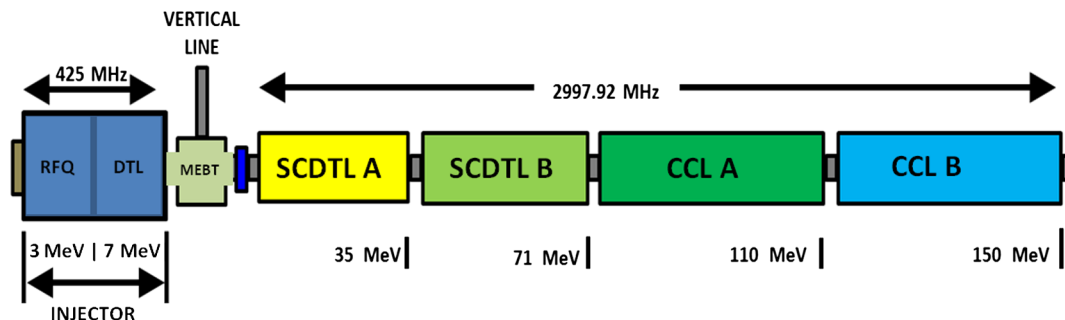


FIG. 1. Schematic layout of the TOP-IMPLART linac.

TABLE I. Main design parameters of the TOP-IMPLART high-frequency (2997.92 MHz) linac.

Subsystem	Parameter	Value
Section 1 (SCDTLA)	Number of modules	4
	Number of tanks per module	9, 7, 7, 5
	Number of cells per tank	4, 5, 6, 6
	Synchronous phase	-19.5°
	Effective shunt impedance (ZT^2)	45–56 MOhm/m
	Accelerating gradient (EOT)	9.8–11.2 MV/m
	rf power loss in the tanks	2.2 MW/m
	Module output energy	11.6, 18, 27, 35 MeV
	Total length	4.81 m
Section 2 (SCDTLB)	Number of modules	4
	Number of tanks per module	5, 5, 3, 3
	Number of cells per tank	7, 7, 8, 8
	Synchronous phase	$-19^\circ, -19^\circ, -15^\circ, -15^\circ$
	Effective shunt impedance (ZT^2)	60–52 MOhm/m
	Accelerating gradient (EOT)	10.6–9.6 MV/m
	rf power loss in the tanks	1.8 MW/m
	Module output energy	45, 55.5, 63, 71 MeV
	Total length	4.96 m
Section 3 (CCLA)	Number of modules	3
	Number of tanks per module	3
	Number of cells per tank	15
	Synchronous phase	-19°
	Effective shunt impedance (ZT^2)	58–64 MOhm/m
	Accelerating gradient (EOT)	15 MV/m
	rf power loss in the tanks	3.6 MW/m
	Module output energy	83, 96, 110 MeV
	Total length	3.57 m
Section 4 (CCLB)	Number of modules	2
	Number of tanks per module	3
	Number of cells per tank	19
	Effective shunt impedance (ZT^2)	67–69 MOhm/m
	Accelerating gradient (EOT)	15 MV/m
	rf power loss in the tanks	3.4 MW/m
	Synchronous phase	-15°
	Module output energy	129.5, 150
Total length	3.14 m	

They are grouped in modules of about 1.5 m length to optimize their mechanical fabrication and installation in the accelerator site. The tanks belonging to the same module have similar internal geometry and the same number of drift tubes. The cells inside a tank (i.e., the distance between the middle of two neighboring drift tubes) have the same length $\beta\lambda$, where β corresponds to the average energy value for that tank. A drawing of two sectional views of SCDTL module 4 is shown in Fig. 2.

As to the mechanical realization, the tanks are composed of three main parts: the central body and a half coupling cavity on each side. These pieces are brazed, forming the

tank. The central drift tubes, all 12 mm in diameter, are supported on axis by two rectangular stems, 180° apart, through which cooling channels are drilled. After a preliminary tuning, the stems are welded to the body. Then tanks are assembled together by welding the two halves of the coupling cavities. The structure is finished by sealing the vacuum ports and the cooling circuit [21].

Single SCDTL tanks operate in zero mode, but the SCDTL structure, as a whole, operates in the $\pi/2$ mode (i.e., zero electric field in the center of the coupling cavities and a shift of π in two consecutive tanks). Thus, the distance between neighboring tanks is set equal to an odd-integer

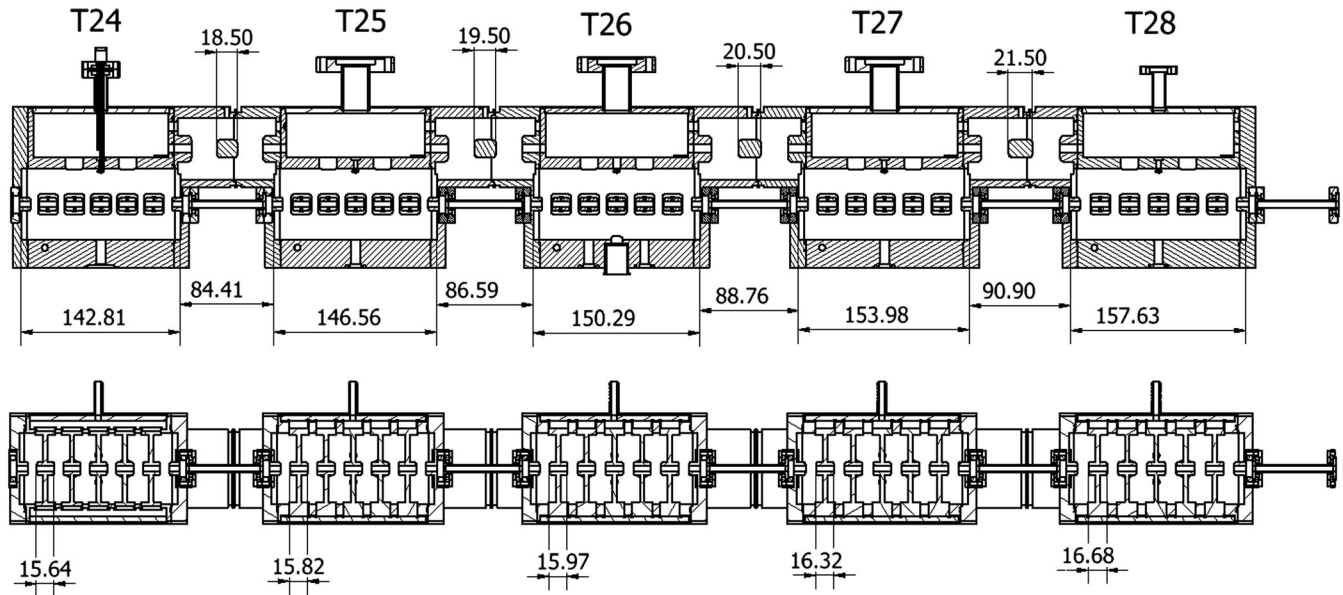


FIG. 2. Two longitudinal sections (top and lateral view) of module 4 with the main dimensions (in millimeters). PMQs are mounted between two neighboring tanks (not shown).

multiple of $\beta\lambda/2$, since they work in phase opposition. The tune is done by operating on tuning screws placed on each accelerating tank and coupling cavity and allows one to reach the operating frequency of 2997.92 MHz in a vacuum at a temperature of about 40 °C. The tuning procedure also levels the amplitude of the average accelerating field of the tanks in the modules ($\pm 2\%$ in field amplitude flatness in the average tank field distribution in a single module). The rf power is delivered to the central tank of each module, where a coupling slot has been designed for critical coupling with the waveguide.

The analysis in terms of accelerating efficiency of the high-frequency structures used in the TOP-IMPLART scheme (see Fig. 16 in Ref. [4]) shows that SCDTL can be usefully employed in the energy range between a few MeV up to roughly 80 MeV. Below this energy, the other competing structure, the CCL composed by side coupled cavities with $\beta\lambda/2$ cell length, has a cell length too short compared to the cavity diameter. This geometry reduces the shunt impedance of the structure and, hence, its efficiency. Above this energy, DTL-like structures show a strong reduction of the average gradient due to the larger cell length $\beta\lambda$.

The study mentioned in Ref. [4] compared ideal SCDTL and CCL geometries. In the practical design of the TOP-IMPLART SCDTL, we decided to minimize the number of rf plants, using 10 MW klystrons for every section of the TOP-IMPLART layout and not exceeding 9 MW for routine operation, and to keep the Kilpatrick factor close to, but not higher than, 1.8 in every structure.

These constraints led to a maximum output energy for the SCDTL segment of 71 MeV. If we had used CCL structures for sections 35–71 MeV, powered with a 10 MW rf plant, the accelerator would have been about 20% longer.

The different choice, done in the LIGHT system, to employ CCL structures already above 37.5 MeV and to use 7.5 MW klystrons all throughout the linac [10] requires four rf plants to accelerate to 70 MeV the 5 MeV injected beam.

III. DESCRIPTION OF THE 35 MeV SECTION

A. Layout and beam dynamics

The part of the TOP-IMPLART linac which is installed and operating at the ENEA-Frascati site is composed of an injector, MEBT, and SCDTLA. Its schematic layout is shown in Fig. 3.

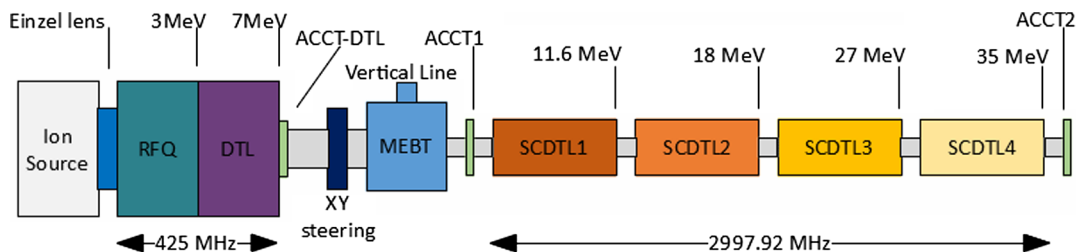


FIG. 3. Schematic layout of the TOP-IMPLART linac up to 35 MeV.

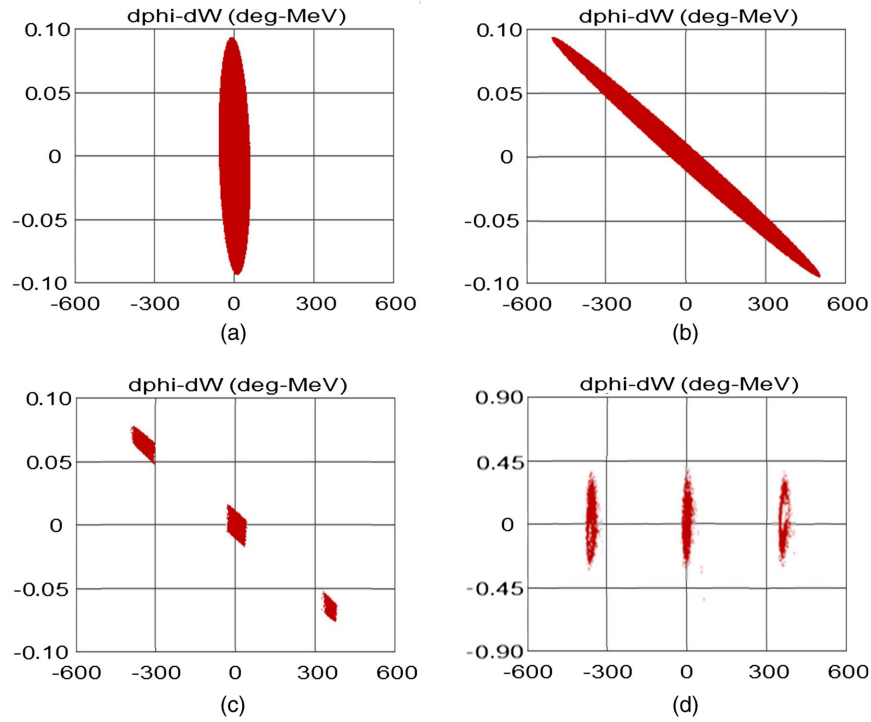


FIG. 4. Computed longitudinal phase space plots: (a) injector exit, (b) SCDTL-1 input, (c) coordinates at SCDTL-1 input of the particles transmitted up to the SCDTL-4 exit, and (d) SCDTL-4 exit.

The beam dynamics has been computed by using the LINAC code [22] tracking 10^5 macroparticles starting from the injector output.

The beam exits the 425 MHz injector with a total phase width of 118° at 2997.92 MHz. The energy spread of ± 93 keV lengthens the proton bunch in the following 2.4-m-long MEBT covering three full rf periods at SCDTL input. The SCDTL phase acceptance is about 57° ($3|\varphi_s|$), and, therefore, only a small fraction of the particles is accelerated to the design energy of 35 MeV. Figures 4(a) and 4(b) show the transformation of the longitudinal phase space from the injector exit to SCDTL-1 input. At this

point, only the particles which are represented in Fig. 4(c) will be transmitted at the output of SCDTL-4 [Fig. 4(d)].

Since the two frequencies (425 and 2997.92 MHz) are not in harmonic relation, they are not locked in phase. The relative phase spans randomly in the range $0-360^\circ$, 425 times in $1 \mu\text{s}$. Figure 4 represents the particular relative phase for which transmission is a maximum.

Computations show that the longitudinal mismatching between the low-frequency injector and the high-frequency linac gives a large amount of losses in the first two SCDTL modules (Fig. 5). This is the only cause of losses, because the transverse emittance of the injector beam (6.6 and

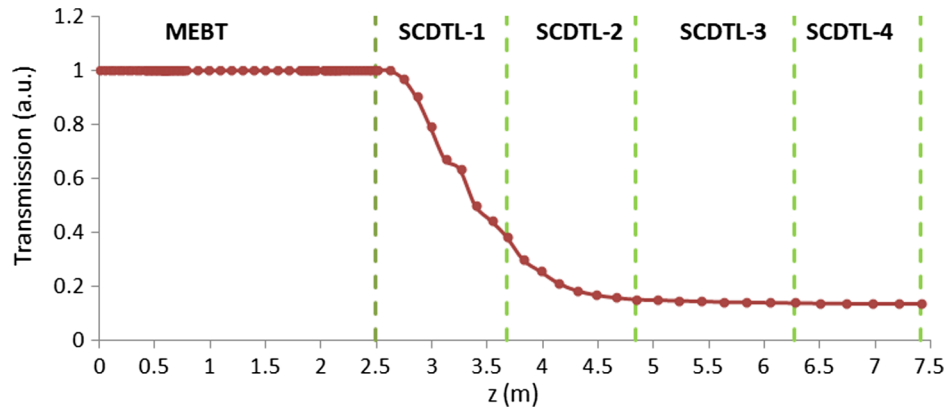


FIG. 5. Computed transmission from the injector output to the SCDTL-4 exit.

7.2π mm-mrad in the $x-x'$ and $y-y'$ plane, respectively) is included in the acceptance of the high-frequency linac ($\sim 9\pi$ mm-mrad). The total transmission from the injector exit to SCDTL-4 output, as computed in the absence of misalignments and other sources of errors, is about 14%. Similar calculations have been performed for all the relative phases between injector rf and SCDTL rf and resulted in $\pm 5\%$ variation of the transmission respect to the average. This behavior does not affect charge stability from one macropulse to another thanks to the averaging process occurring in the pulse.

Figures 6 and 7 show the evolution of the envelopes and emittances computed with the relative phase for maximum transmission. The beam is transported without losses in the MEBT, where the beam pipe diameter is 35 mm. The four quadrupoles are set to match the beam emittance to the acceptance of the SCDTL, where the beam pipe diameter becomes 4 mm in the first two modules, 6 mm in the intertank space, and 5 mm in the last two modules.

The evolutions are strongly determined by the large number of losses occurring in the first stages of acceleration at a high frequency; only after the second module, when the beam starts to be transported practically without losses and the current is definitively stabilized, do the computed parameters become really representative of the beam.

The plot of Fig. 7, concerning the longitudinal plane, represents the evolution of a single bunch produced by the injector at 425 MHz [Fig. 4(a)]: It has to be considered that, when the beam propagates in the high-frequency structures, the longitudinal emittance is scarcely meaningful, because the original bunch is split in three subbunches temporally separated by a 3 GHz period [Fig. 4(d)], each with a longitudinal emittance around 1π deg-MeV.

More details on the general characteristics of beam dynamics in the TOP-IMPLART linac, including tolerances on mechanical realization and misalignments, can be found in Ref. [8]. However, some aspects have been further analyzed to support the commissioning phase of the first section of the accelerator. In particular, the variability in the injection energy and the rf phase and amplitude stability strongly affect the output beam characteristics. Thus, a dedicated set of simulations has been performed to investigate the behavior of the machine up to 35 MeV, in order to set accuracy and stability limits for those parameters. The output beam sensitivity to one single source of error has been determined to evaluate each individual contribution. In this analysis, only particles transmitted with an energy larger than 34 MeV are considered.

The sensitivity of the output intensity to the injection energy error is shown in Fig. 8. An error on the injection energy

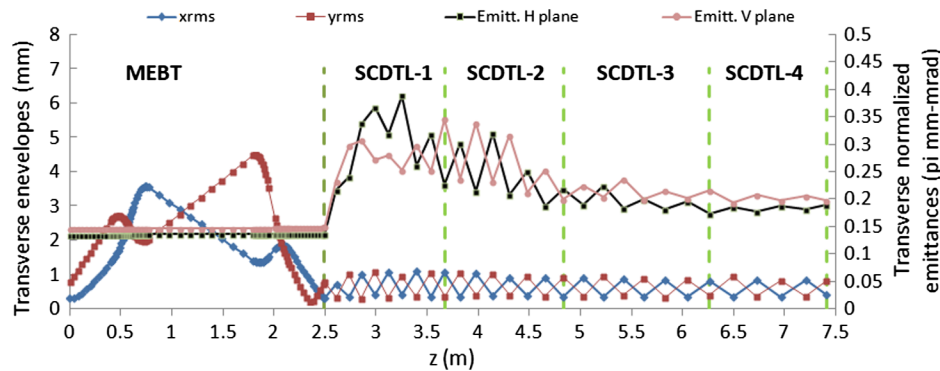


FIG. 6. Computed rms transverse envelopes and emittances from the injector exit up to the SCDTL-4 output.

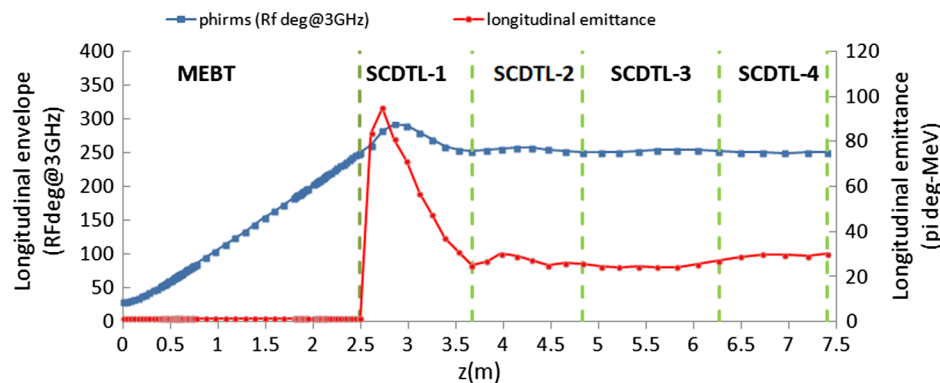


FIG. 7. Computed rms longitudinal envelope and emittance from the injector exit up to the SCDTL-4 output.

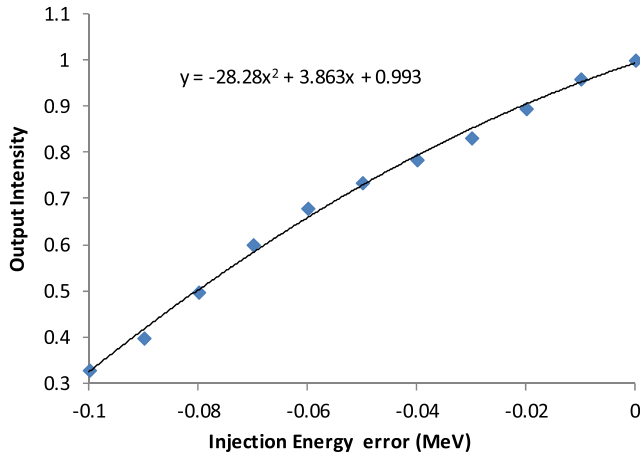


FIG. 8. Computed output intensity normalized to the maximum value versus the injection energy error (the black line is a second-order polynomial fit to the computed data).

of 20 keV (the reference being 7 MeV) produces an output current drop of 10%.

This study was done keeping the booster parameter fixed to the nominal values with the aim to monitor only the effect of the pulse-to-pulse injector field stability on the output current. The error studies also indicate that an injector lower field can be only partially compensated by increasing the power on the first SCDTL module: A 6.95 MeV injector beam produces a 25% drop in the output current, which can be decreased to 20% by a 10% increase of the rf power at SCDTL-1 input. This feedback can be managed by the control system only on a 10-s timescale, incompatible with a pulse-to-pulse adjustment; therefore, it is mandatory to rely on the injector field stability.

The influence of the rf field amplitude and phase in the SCDTL modules on the output beam has also been investigated. As described in the following paragraph, the klystron power is divided in two branches, feeding two modules each, with a splitter placed before each couple to balance the power in the single module. In order to evaluate numerically the sensitivity to rf field amplitude errors, the analysis has been done separately in the two branches: Five separate groups of runs (30 runs in each group) have been done, randomly varying in a defined range the field amplitude in one pair of modules and keeping the other pair fixed to the design values.

The results in terms of output intensity and energy variation for each group of runs have been reported in Table II. It can be observed how the sensitivity to this parameter decreases when the energy increases, meaning that larger tolerances on rf amplitude stability can be accepted at higher energies. For this segment of the accelerator, a precision better than 0.5%, corresponding to a klystron rf power stability of 1%, is required to keep the maximum intensity variation below $\pm 5\%$. The major

TABLE II. Effects on the output beam of rf amplitude errors in SCDTL modules.

SCDTL modules	Amplitude error	Intensity variation	Energy (MeV)
1-2	$\pm 0.5\%$	$\pm 4\%$	35.01 ± 0.01
1-2	$\pm 1\%$	$\pm 9\%$	35.02 ± 0.02
1-2	$\pm 2\%$	$\pm 22\%$	35.03 ± 0.04
3-4	$\pm 0.5\%$	$\pm 2\%$	35.01 ± 0.01
3-4	$\pm 1\%$	$\pm 7\%$	35.00 ± 0.04

contribution to intensity variation come from the first two SCDTL modules.

The rf phase can be controlled separately on the last three modules. The effect of a phase error on each single module has been computed by a phase scan in a range of $\pm 5^\circ$ rf with respect to the module reference value. In the considered range, the output beam intensity decreases by 9% and 5% for a phase error on SCDTL-2 and on SCDTL-3, respectively. The beam intensity is only weakly affected by a phase error on SCDTL-4, as this is the output module in the present layout.

B. Linac operation

A picture of the 35 MeV linac section currently in operation at ENEA Frascati is shown in Fig. 9.

The injector, originally designed for radioisotopes production [15], consists of a 2.3-m-long RFQ and a 1.5-m-long DTL. The protons are extracted from a Duoplasmatron source (with a maximum extraction voltage of 30 kV) and are focused by an einzel lens into the RFQ. The RFQ accelerates the beam up to 3 MeV and the DTL up to 7 MeV.

A copper aperture is inserted to limit the proton source current (10 mA) to a maximum value of 1.5 mA. The current from the injector can be varied by controlling either the extraction voltage or the einzel lens voltage [23].



FIG. 9. TOP-IMPLART 35 MeV segment currently in operation.

The injector control electronics provides feedback loops in the source and in the rf amplifier to stabilize the output beam. The rf amplifier of the RFQ and DTL operates in a closed loop with active feedbacks on the amplitude, frequency, and phase.

The stability of the injector can be monitored on-line. A subset of the available signals is sampled, each pulse at the same time, using sample and hold amplifiers. The sampling time can be varied to scan different parts of the pulse. The sampled value is digitized and recorded to build a time chart and is available for further off-line analysis. The injector stability affects the minimum stability achievable at the accelerator output. The measured maximum arc voltage variation is about $\pm 2\%$, while it is $\pm 0.02\%$ for RFQ and DTL fields. Figure 10 reports an example of stability measurements performed in a time frame of 120 s on the arc signal (top) and the DTL signal (bottom). The former is relevant to assess the minimum variation expected on the current injected in SCDTL-1. The latter, instead, mainly affects the transmission from the input to the output of the high-frequency linac, being correlated to the energy of the injected beam.

Two different injector and MEBT settings are used for beam extraction on the vertical line or injection into SCDTLA. In the first case, the injection energy can be varied between 3 and 7 MeV [24] to perform “in vitro” radiobiology experiments. In the latter, it is fixed to the design energy for acceleration through the high-frequency booster of 7 MeV.

The operation of the SCDTLA section is driven by the rf power distribution network shown in Fig. 11. It is based on variable elements (power dividers, 3 dB hybrids, and phase shifters) that allow precise and independent amplitude and phase control for the four SCDTL structures.

The Low Level RF signal is generated by a synthesized source, amplified and delivered to a 10 MW peak power Thales TH2157A-II klystron, driven by a solid state

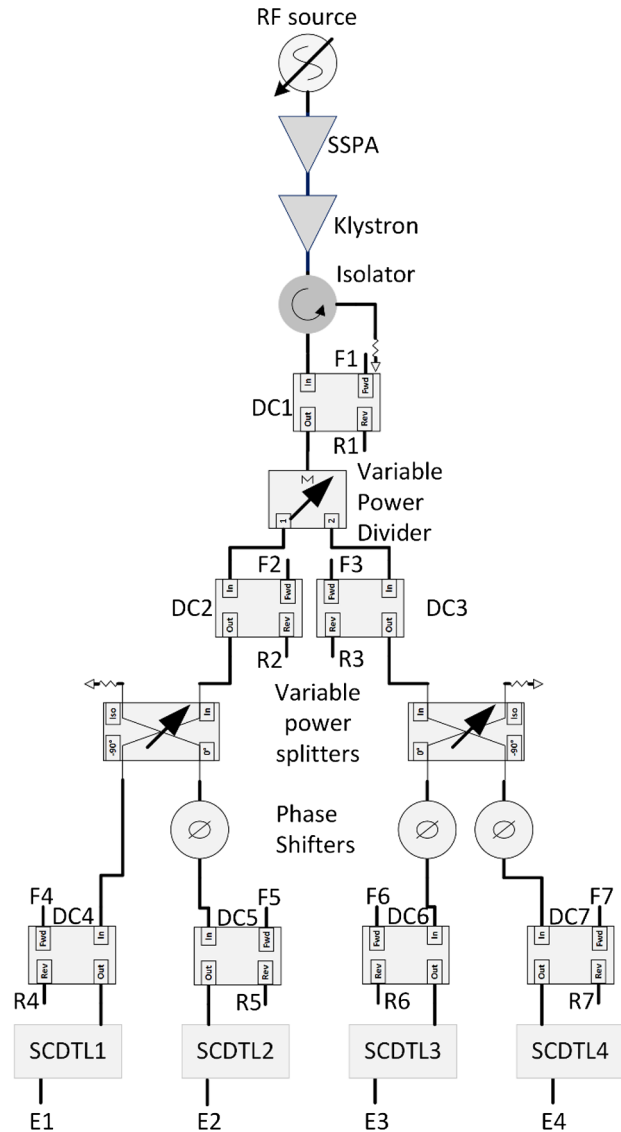


FIG. 11. The rf power system distribution scheme.

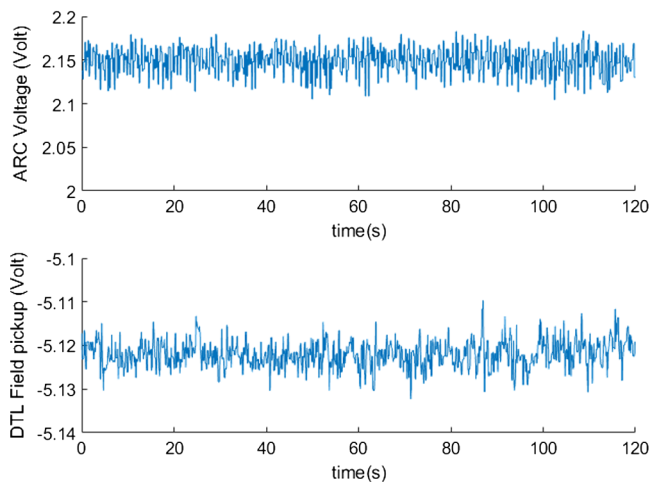


FIG. 10. Arc (top) and DTL (bottom) signals versus time.

Scandinova K1 modulator. Directional couplers (identified in Fig. 11 by “DC” followed by a number) are installed in each branch of the waveguide network monitoring forward and reflected power. DC1 is used to measure the rf power after the circulator in the accelerator bunker, that is also the input power to the variable power divider. This component splits the input power between the first pair of structures (SCDTL-1 and -2) and the second pair (SCDTL-3 and -4). The power divider can steer all the input power between its output ports, although the power ratio is rarely adjusted during machine operation. The DC2 and DC3 couplers monitor the output power from the divider, that is, the input to the variable 3 dB hybrids (variable power splitters in Fig. 11). The 3 dB hybrids, designed by ENEA following Ref. [25], set the power delivered to each structure. The three phase shifters are required to set the relative phase of the rf at the input of each structure, SCDTL-1 being the

TABLE III. Main rf parameters of the SCDTL structure.

Module	Power (MW)	Q0
SCDTL-1	1.3	6916
SCDTL-2	2.2	8446
SCDTL-3	2.4	9163
SCDTL-4	2.12	11222

phase reference. The three phase shifters are of dielectric-slab type and have been realized on a custom design to provide a differential phase shift of 100° .

Absolute rf power measurements are performed using a power meter equipped with a peak and an average power sensor. The measured power consumed by the four SCDTL structures is reported in Table III together with the Q values. The total power needed to excite the rf fields into the SCDTLA section, for normal operations, amounts to 8 MW. This value is reached with a klystron power output of 9.1 MW. Waveguide losses amounts to 1.1 MW (12% of the total).

Pick-ups are inserted in each structure (referred to as E1, E2, E3, and E4 in Fig. 11) sensing a signal proportional to the amplitude of the electric field, which is subsequently read off by a peak detector. The traces of these signals are stored as a reference in the oscilloscope memory at a nominal energy and maximum beam current. The actual signals are monitored during the operation and compared with the reference ones to perform the necessary adjustments.

In order to keep the electric field amplitude and phase error to a minimum, as required by beam dynamics, each of the four SCDTL modules is provided with a thermocontroller that keeps the temperature at the proper value. The temperature of each structure is measured by a PT100 sensor placed on a suitable point on the copper surface. Because of differences in the manufacturing process, the four structures reach the target frequency at 49°C , 38°C , 52°C , and 36°C , respectively. The chillers used for the preliminary tests [26], made by simple 2 kW heater-fan devices, have been recently replaced by chillers based on Peltier elements. Their use allows a high-precision temperature control reaching $\pm 0.02^\circ\text{C}$ for all structures in stationary conditions, strongly improving the long-term stability. The capability of the thermocontrollers to recover the reference temperature when the average rf power changes has been tested by varying the repetition frequency in the range 10–100 Hz. In this case, the maximum measured temperature transient is below 1.2°C . This shift can be compensated by inserting a 4-mm-diameter copper rod in the central tank of each structure. The resonance frequency can be shifted by 70 kHz, a value that can compensate more than 1°C of temperature error. The frequency feedback on SCDTL modules consists of an automatic frequency control driving the tuner. The system, described in Ref. [27], is able to compensate the frequency

TABLE IV. Average on field pick-up value for the four SCDTL structures and relative error.

Module	Field pick-up (mV)	Instrument error (%)
SCDTL-1	114.81	± 0.34
SCDTL-2	75.26	± 0.52
SCDTL-3	77.57	± 0.50
SCDTL-4	136.84	± 0.29

drifts induced by temperature oscillations that can occur during the transient when the rf power is switched on or if the average power is varied. This double regulation system allows a fine-tuning (< 1 kHz) of the structure in any operational condition.

The stability of klystron rf power and of electric field amplitude in the different sections of the accelerators has been evaluated from rf pulse envelope digitalization. The rf waveforms of the forward and reflected power are detected using calibrated zero-bias Schottky diodes and delivered to the diagnostic system. Additional attenuation is placed in front of each diode to reduce the power level at its input. This additional attenuation has the dual function of bringing the rf power level within diode detection dynamics and to read all output voltages within one decade (for nominal levels). The latter is necessary to reduce as much as possible the effects of diode nonlinearity, delivering to their inputs signals in the same power range. The output voltage signals, corresponding to pulse envelopes, are transmitted to the control room using standard RG58 coaxial cables and sampled using synchronized Picoscope 3405D digitizers. Each digitizer is programmed to acquire traces made of 2000 samples, each in a time span of $8\ \mu\text{s}$ (corresponding to a sample time of 4 ns), which are recorded in its internal memory. The level of the pulse flattop is obtained from the average of 240 points for each

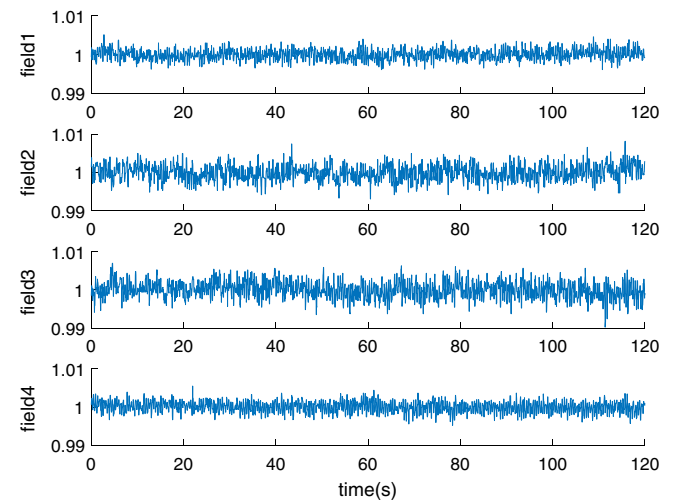


FIG. 12. Electric field pick-up signal in the four SCDTL modules versus time.

sample, corresponding to 25% of its full width. The main source of error is given by the instrument (8-bit resolution, 200 mV input voltage range) sampling error $\Delta/2$ with $\Delta = 200/256=0.78$ mV. Table IV reports the average value of the field pick-up output signal recorded in 120 s and the corresponding percentage error.

Figure 12 shows the four pick-up output signals (normalized to the average value on the flattop of the pulse), which are proportional to the electric field amplitudes in the four SCDTL structures. The maximum variation of the fields remains within $\pm 0.5\%$, that is comparable with the instrument precision. These results are compatible with the required tolerances on field amplitude precision reported in Table II.

C. Beam monitoring

Measurement of the proton beam current and charge includes two different types of diagnostics, optimized for different current ranges. The first type, typical of the accelerator field, is based on both noninterceptive (current transformer) and interceptive [Faraday cup (FC)] monitors. These devices provide detectable signals for beam currents in the range of 5–50 μA .

At lower intensities (which are typical of radiobiology and radiotherapy applications, with doses in the range of 1–10 GV), dedicated detectors for radiation dosimetry (ionization chambers) have been implemented. These are specifically designed to control the delivered dose also on each pulse.

1. High-current diagnostic tools

The main diagnostic tools used in the actual TOP-IMPLART accelerator have been shown in the schematic layout of Fig. 3. The beam current at the entrance and at the exit of the high-frequency linac is measured by two identical ac current transformers (referred to as ACCT1 and ACCT2 in Fig. 3). These are produced by BERGOZ Instrumentation, equipped with calibrated amplifiers to obtain an overall gain of 1 V/mA over a 1 M Ω load, with a negligible droop for microsecond-duration pulses. The output transformer is placed in air and can be moved following the accelerator assembly progresses. The length and the bore hole diameter (20 and 6 mm, respectively) have been realized according to ENEA specifications, in order to fit in the linac available space.

The beam current is also measured by a custom designed Faraday cup. The signal generated by the Faraday cup is amplified by a FEMTO DHPCA-100 current amplifier, configured for a nominal transimpedance gain of 10^4 V/A on a 50 Ω load. The actual gain accuracy is $\pm 1\%$.

2. High-sensitivity charge detectors

Two thin integral ionization chambers (IC_A and IC_B) and one multistrip chamber (IC_2D), that measures the

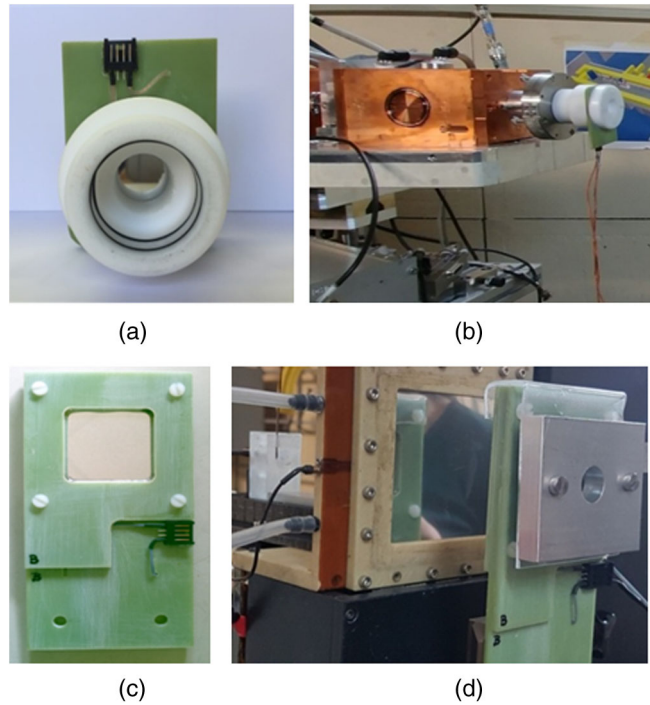


FIG. 13. (a) Ionization chamber IC_A, (b) IC_A mounted at the exit of SCDTL-4 after ACCT2, (c) front view of ionization chamber IC_B, and (d) IC_B mounted after a collimator during an irradiation session at the end of the beam line in air.

beam position and intensity profile of each beam pulse [28], are specifically designed and developed for the TOP-IMPLART beam. These are high-sensitivity devices able to detect a charge as low as 1 pC/pulse. The two integral chambers operate at a bias voltage of 250 V (variable) and are realized with aluminized Mylar electrodes (12 μm Mylar, 4 μm aluminum) spaced by 2 mm of air. They have different geometries and mechanical supports: IC_A is designed to fit at the exit of the beam pipe [Figs. 13(a) and 13(b)], while IC_B can be placed anywhere along

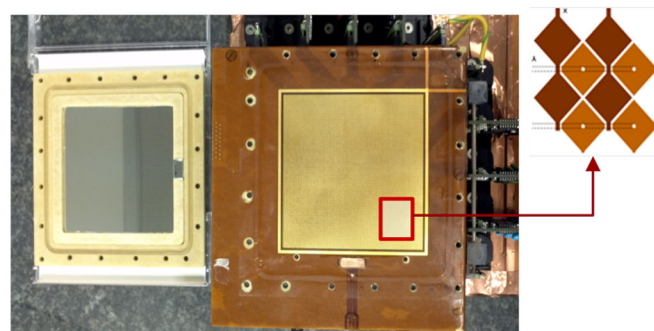


FIG. 14. Multistrip IC-2D chamber prototype components: (left) the anode aluminized Mylar window glued on the glass fiber epoxy Permaglas frame; (center) the segmented cathode made by a layer of kapton and copper pads connected by strips along x and y (upper-right drawing).

the beam axis beyond the accelerator exit in air [Figs. 13(c) and 13(d)].

The IC.2D ionization chamber, shown in Fig. 14, is made of a highly segmented striplike cathode that exploits the micropattern technology.

The chamber measures the single beam pulse intensity profiles simultaneously along the x and y axes, with spatial resolution at the level of 0.3 mm (strip pitch 0.875 mm), with a sensitivity of 100 fC and a dynamic range larger than 10^4 . This is obtained by means of a dedicated electronics that automatically adapts the gain on each segment (channel) according to the amount of collected charge.

3. Photoluminescence of color centers in LiF crystals for Bragg peak detection

Commercially available (10×10) mm², 1-mm-thick polished lithium fluoride (LiF) crystals are used as passive detectors for proton beam imaging [29]. Protons lose energy in the crystal and create F_2 and F_3^+ aggregate color centers, stable at room temperature, which emit red and green photoluminescence (PL), respectively, under optical excitation in the blue spectral range [30]. By using a fluorescence microscope equipped with a camera, the visible fluorescent proton beam transversal spatial image stored in the irradiated LiF crystal is acquired. When the LiF crystal is positioned with the polished faces parallel to the beam propagation direction (see Fig. 15), as the PL intensity is proportional to the energy lost by protons in the crystal, the beam energy is obtained by comparing the

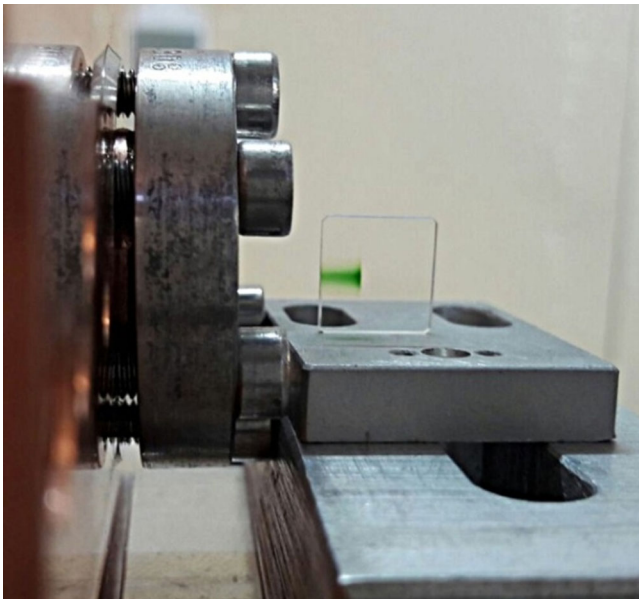


FIG. 15. LiF crystal positioned after the current monitor ACCT2 with the polished faces parallel to the beam propagation direction just after proton irradiation. The green coloration, observed by the naked eye, is due to the broad absorption bands of proton-induced aggregate color centers.

measured distance between the crystal edge and the PL intensity peak, in the fluorescent image of the Bragg curve, to the value obtained by the SRIM code [31] in the same experimental conditions, as explained in detail later.

IV. BEAM COMMISSIONING RESULTS

A. Characterization of the beam at SCDTL-4 output

The measurements reported in this section have been done at a repetition frequency of 25 Hz. However, the linac operation has been successfully tested up to 50 Hz. The increase of the repetition frequency up to 100 Hz is limited by the heating of the power steering components in the rf network, not yet equipped with an adequate cooling system for high-rate operation.

1. Beam intensity

The pulse output current can be set in the range of 0–50 μ A, controlling the injector current by varying the voltage on the einzel lens. Figure 16 shows the beam current pulse at the input and output of the four SCDTL sections; all the machine parameters are optimized in order to accelerate the maximum current. They are measured respectively by the ACCT1 (yellow curve) and ACCT2 (blue curve). The output current is also measured by the Faraday cup (green curve). In front of the FC, a slab of 3.5 mm of aluminum is inserted to stop all the particles with an energy lower than 34 MeV.

The PMQ lattice in SCDTL-4 is able to transport the beam coming from SCDTL-3 even in the absence of acceleration. This feature is exploited during the commissioning to find the optimal settings of SCDTL-4 parameters (in particular, the rf phase). In Fig. 16, the signals of ACCT2 and FC are on the same beam current scale (10 μ A/div). This means that all protons in the 50 μ A

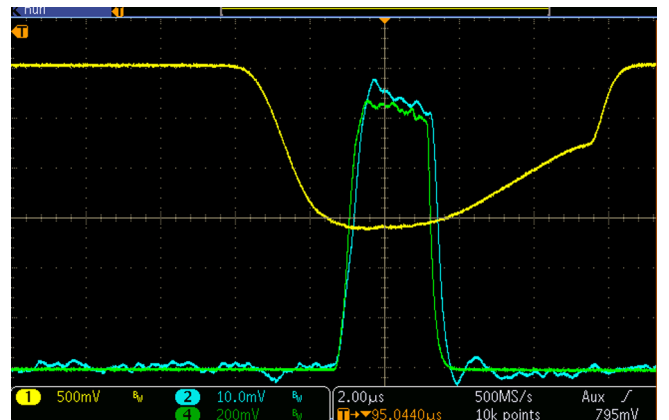


FIG. 16. Oscilloscope signals: Injected current in SCDTL-1 read by ACCT1 (yellow trace, 500 mV/div), SCDTL-4 output current read by ACCT2 (blue trace, 10 mV/div), and FC (green trace, 200 mV/div). The horizontal scale is 2 μ s/div.

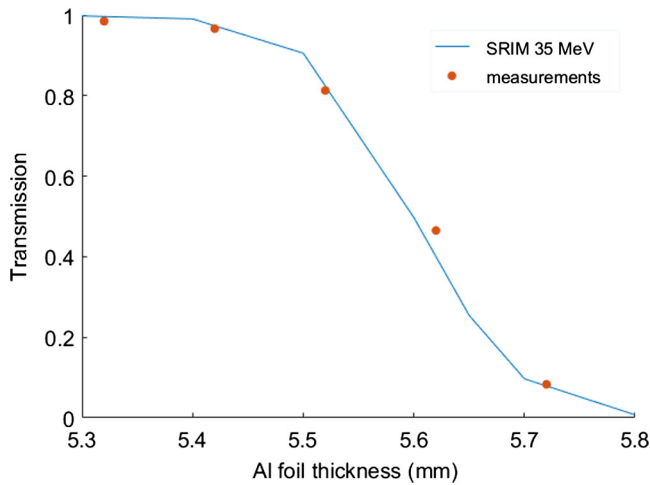


FIG. 17. Beam current transmission in aluminum: Experimental data and computed curve for 35 MeV protons.

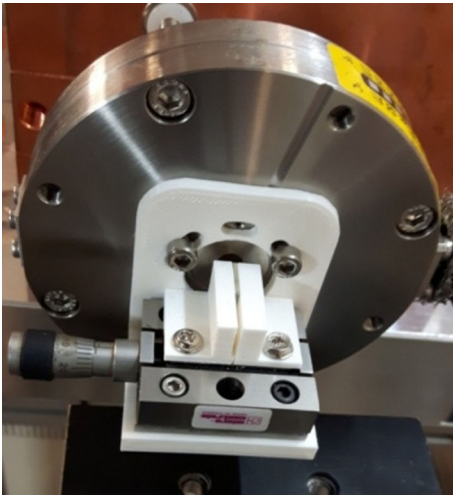
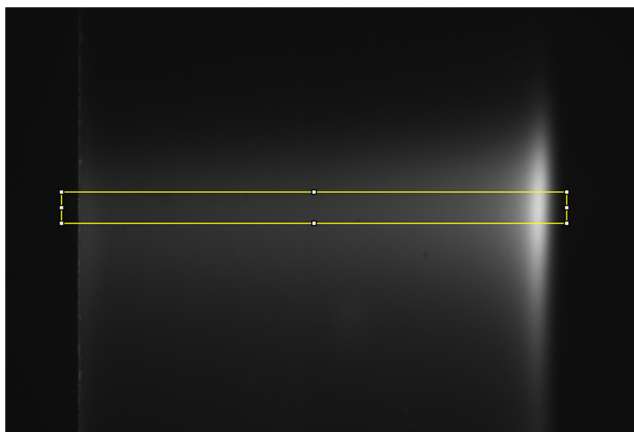
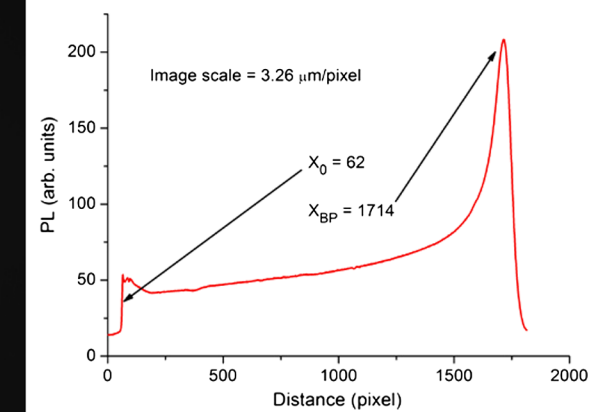


FIG. 18. LiF crystal positioning system for beam energy measurement at the SCTDL-4 output.



(a)



(b)

FIG. 19. (a) Bragg curve PL image stored in the LiF crystal placed at the exit of SCTDL-4 and (b) PL intensity profile versus depth in the selected yellow rectangular region.

pulse exiting from the linac are properly accelerated by SCDTL-4, since the levels of the flattop of the two signals match. The difference in the rise and fall time of the pulses, with the ACCT2 characterized by a higher rise or fall time compared to the FC (570 ns), depends on the bandwidth of the amplification electronics.

2. Beam energy

The output beam energy is evaluated from the proton range in aluminum, measuring the beam current transmission through calibrated aluminum slabs of increasing thickness. The Faraday cup is used for this measurement. Figure 17 reports the measured data compared with the curve computed by the SRIM code for a 35 MeV proton beam after the passage in the linac exit window (50- μ m-thick Ti foil).

A more accurate beam energy measurement has been performed off-line, determining the Bragg peak position in the fluorescent image stored in the proton-irradiated LiF crystal. Figure 18 shows the LiF crystal holder used for this measurement, placed at a distance of 5 cm from the exit window of SCDTL-4 after the current transformer ACCT2.

Figure 19(a) shows the visible PL proton beam fluorescent image stored in a LiF crystal after a 9-s-long irradiation (particles coming from the left side of the picture). The image has been obtained by a Nikon Eclipse 80-i fluorescence microscope equipped a 2 \times objective (image scale = 3.26 μ m/pixel) and an Andor NEO s-CMOS camera under blue excitation with a filtered Hg lamp. Figure 19(b) shows the PL intensity profile of the selected central image region [130 \times 1800 pixel yellow rectangle in Fig. 19(a)] where the beam shows the maximum PL intensity.

The position of the Bragg peak (X_{BP}) retrieved from the image is at $5386 \pm 13 \mu$ m from the crystal edge (X_0), corresponding to a beam energy of 35.09 ± 0.03 MeV.

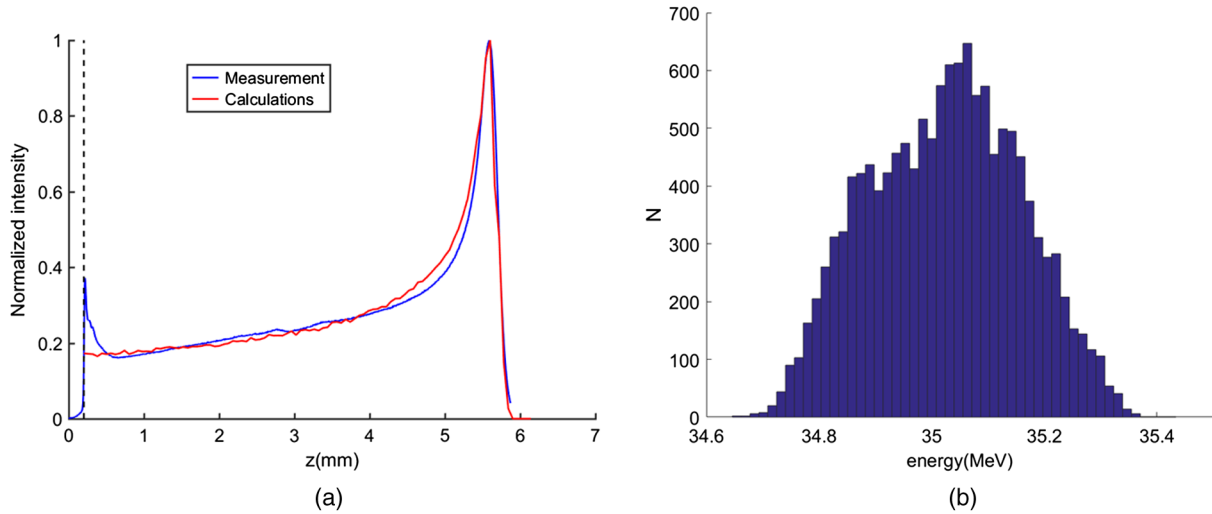


FIG. 20. (a) Comparison between the measured PL intensity profile versus depth and the computed energy loss profile in the LiF detector. The dotted line indicates the crystal edge. (b) Computed beam energy distribution of the accelerated beam before the exit window.

The uncertainty is due to the size of the single pixel (± 1 pixel) summed to the uncertainty of the estimated position of the crystal edge (± 3 pixels), giving a total error of ± 4 pixels multiplied by the image scale. The measurement has been compared with beam dynamics calculations performed in two steps. In the first step, the LINAC code has been used for the beam tracking in a vacuum through the accelerator up to SCDTL-4 output. In the second step, the six-dimension phase space of the particles computed by LINAC has been used as input of the SRIM Monte Carlo code. SRIM transported the particles through a sequence of layers: a 50- μm -thick titanium window, a 5-cm-long path in air, and finally the LiF crystal, replicating exactly the experimental conditions.

Figure 20(a) shows the very good agreement between the measured PL intensity profile in LiF [obtained by integrating the PL signal through the whole vertical beam dimension in the image in Fig. 19(a)] and the computed ionization energy loss curve. Figure 20(b) shows the computed energy spectrum of the beam in a vacuum at the accelerator output immediately before the titanium window.

In the computation, the electric field amplitude in SCDTL-3 and SCDTL-4 has been increased by 1% with respect to the reference value to match the measurement. This explains an energy value slightly larger with respect to the design value of 35 MeV as shown in Fig. 20(b).

3. Beam transverse size

The on-line imaging of the beam spot is performed with an alumina fluorescent screen, placed after the vacuum window, and a Basler ACE camera with a monochrome 12-bit CCD sensor, used to digitally acquire the spot position and size. The CCD sensor size is 3.7 mm \times 2.8 mm with a pixel dimension of 5.6 μm \times 5.6 μm . The camera is hardware triggered for synchronous acquisition

and exposure control. Figure 21 shows the measured beam spot: The elliptical spot shape is determined by the last PMQ that focuses the beam horizontally.

4. Calibration of charge monitors

The Faraday cup was calibrated on a bench by measuring the capacity of the circuit through a 4.3 μs pulse of known amplitude, obtaining a calibration factor of 56.5 pC/100 mV. The FC was used to calibrate the integral ionization chambers (ICs); both FC and IC signals are integrated by two identical integrator circuits.

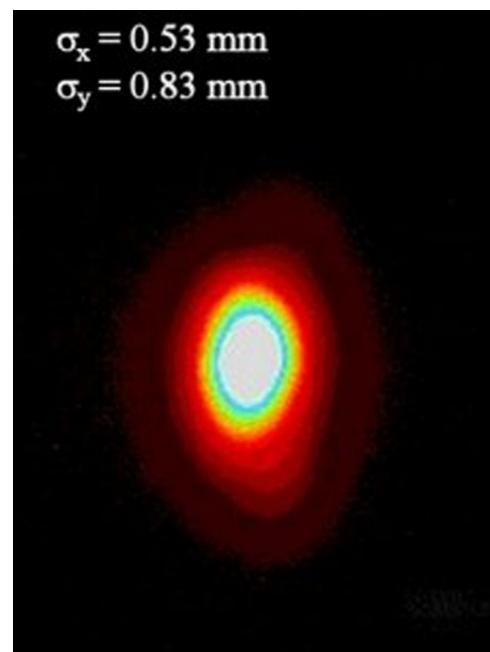


FIG. 21. Measured beam spot at the linac exit.

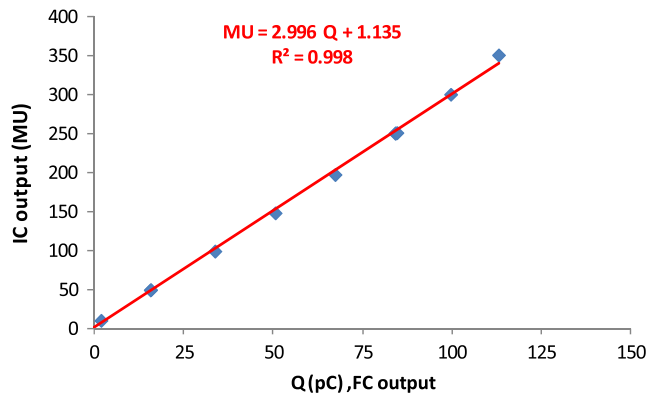


FIG. 22. IC_B output in MU versus the charge measured by the FC. The red line is a linear fit, with parameters quoted in the plot text.

The ionization chambers monitor the dose delivered by the beam. Their output is commonly expressed in monitor units (MU), an arbitrary unit generally used in clinical accelerators to indicate the output dose in the specific delivery geometry. As the dose is equal to the linear energy transfer multiplied by the particle flux, this means that at a fixed energy the output of the ICs gives a measure of the output beam charge. In order to calibrate the ICs at the linac exit, two aluminum circular collimators (10 mm thick, 13 mm diameter) were placed before the chamber and in front of the FC, assuring that the two monitors intercept the “same” beam (assuming the effect on the beam produced by the ionization chamber to be negligible). The output of FC and IC has been compared for different output beam intensities, varying the current in one of the steering magnets placed in the MEBT. The resulting calibration curve in a range up to 113 pC is reported in Fig. 22, where the response of IC_B is given in terms of monitor units and the response of the Faraday cup is given directly in pC.

The relationship between the two monitors is linear, showing the absence of saturation effects of the ionization chamber in the explored range of beam intensities.

5. Output charge stability

The stability of the charge delivered by each pulse is of utmost importance. It affects the stability of the dose delivered to the patient. Consequently, it defines the number of repaintings needed to obtain the accuracy established by the quality assurance protocol in the dose delivered by a scanned beam. A difference between the measured and the planned dose within $\pm 5\%$ is accepted [32,33].

In the TOP-IMPLART linac, the stability of the accelerated charge per pulse is constantly monitored during the operation of the machine, recording the output of the two integral ionization chambers previously described.

As a measure of output charge stability, we use the coefficient of variation $CV = \sigma_Q / \langle Q \rangle$, that is defined as the

TABLE V. Output charge stability measurements.

MU	CV (%)
30	3.5
50	2.9
60	3.3
90	2.9
150	3.2
200	2.1
250	1.8
350	2.3

ratio between the standard deviation and the average value of the charge in N measurements. Table V reports the value of this parameter in a range of MU between 30 and 350, corresponding to an interval of output charge between 10 and 116 pC. The values of CV are computed on $N = 3000$ measurements for each MU value. These measurements show a reproducibility of the output charge between 2% and 3.5% in the whole range, including the uncertainties and fluctuations of the ionization chamber.

6. Summary of main beam parameters

From the commissioning, the main output parameters of the first TOP-IMPLART section are summarized in Table VI.

B. Characterization of the broad beam

During the commissioning, satellite measurements have been performed in view of the beam dosimetric characterization [34] required for in vitro and in vivo radiobiological studies. Moreover, experiments in the fields of spectroscopy and preservation of cultural heritage [35–37] have also been carried out. These experiments typically require a homogeneous beam on a circular area of 1–2 cm². As an active scanning system has not yet been implemented, this broad beam is obtained by free expansion in air of the protons exiting from the accelerator pipe. Figure 23 shows the x-y raw cumulated beam profiles measured by the IC_2D monitor at the reference position of

TABLE VI. List of the main parameters of the 35 MeV section.

Parameter	Value
Pulse length (FWHM)	2.7 μ s
Repetition frequency	25 Hz (typical) 50 Hz (max)
Beam (pulse) current	$\leq 50 \mu$ A
Output charge per pulse	135 pC (max)
Output number of particles per pulse	8.4×10^8 (max)
Output energy	35 MeV
Beam size (FWHM)	<1 mm in x <2.5 mm in y
Output charge stability (1 sigma)	$\sim 3\%$

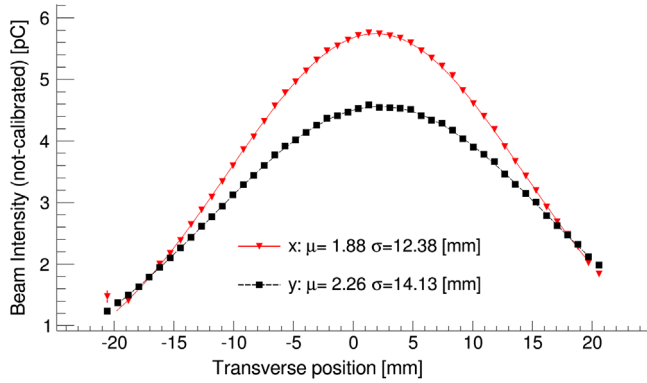


FIG. 23. X-Y raw profiles measured by the IC_2D chamber at 160 cm from the linac and corresponding Gaussian fits. The beam intensity is the average on 660 beam pulses.

160 cm from the beam pipe exit window; the beam spread is estimated by the Gaussian fits σ_x and σ_y , which are reported in Fig. 24 as a function of the distance traveled by the beam in air.

Part of the commissioning has been dedicated to characterize the beam in this position, by using the IC_2D chamber and the two integral chambers IC_A and IC_B at the output of the linac and 8.5 cm before IC_2D, respectively. A cylindrical hole collimator, 16 mm in diameter, is placed right before IC_B. Chambers and collimator are aligned with the output flange of the linac. During the irradiation, the IC_A chamber reads the charge at the exit of the accelerator and IC_2D measures the shape, the intensity, and the centroid position (as shown in Fig. 25). The beam is switched off when IC_B reads a preset cumulative charge. This procedure has been validated through an experimental campaign [34,38], aimed at evaluating the reproducibility of the dose delivered by the whole system (accelerator and beam control monitors). These measurements have been done also comparing the responses of different types of calibrated dosimeters positioned at 180 cm from the linac exit.

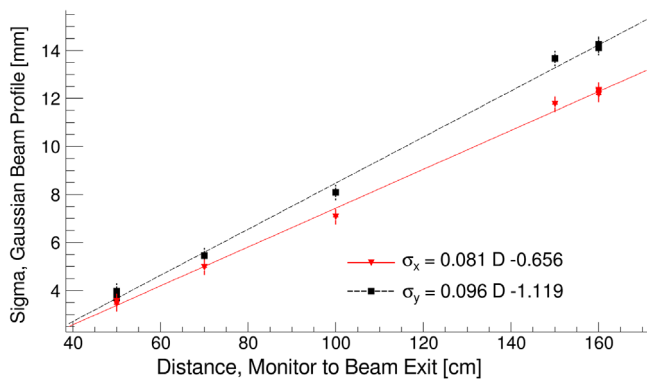


FIG. 24. Beam spread measured by IC_2D along x and y as a function of the distance from the beam pipe exit window (the distance traveled in air by the beam); reported σ_x and σ_y from the Gaussian fit (as in Fig. 22).

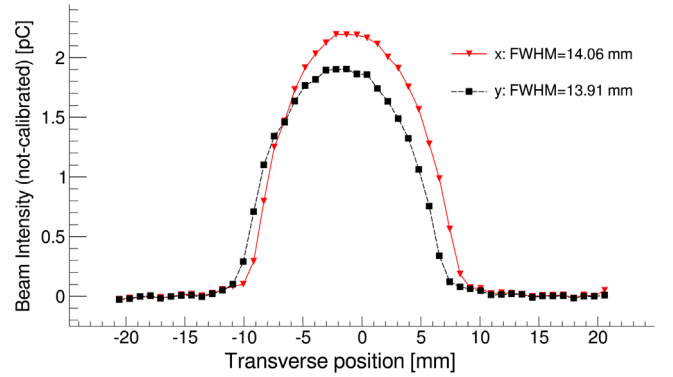


FIG. 25. Raw intensity profile (single pulse average) of the beam freely traveling 160 cm in air and passing through a 16-mm-diameter collimator, 8.5 cm before IC_2D.

The charge or pulse has been controlled by the voltage on the einzel lens (between 25.7 and 28.7 kV at an extraction voltage of 28.1 kV) at a fixed dose of 4 Gy, with irradiation durations, respectively, between 16 and 106 s and a charge or pulse between 1 and 6.5 pC. Results show a homogeneity of the beam, within 2.6% in a 16-mm-diameter circular surface and a reproducibility of the dose better than 3.5%. A detailed description of these measurements and of the experimental setup is reported in Ref. [38].

Since protons lose a portion of their energy traveling in air, the beam energy has been measured also at 1.8 m from the linac exit by a LiF crystal, as described previously. The retrieved position of the Bragg peak was at (4362 ± 13) μm from the crystal edge, corresponding to an energy of (31.00 ± 0.03) MeV. This result is in agreement with beam tracking calculations, taking into account the beam dynamics in the accelerating structures and the interaction of the beam with the different encountered materials: titanium window, air, and the IC-2D chamber (equivalent to 0.17 mm of water and decreasing the energy of 290 keV). The range in water at the measured beam energy is 9.22 mm.

V. CONCLUSIONS AND FUTURE WORK

The 35 MeV section of the TOP-IMPLART linac has been successfully commissioned. This represents the first step in the development of a 150 MeV linear accelerator for proton therapy at ENEA Frascati Research Center. Additional SCDTL sections are under construction, to reach the clinically valuable energy of 71 MeV. The commissioning has been carried out using diagnostic tools belonging to the particle accelerator community but also devices commonly used for characterization and monitoring of clinical beams. This combined approach provides the first demonstration of the capability of a full linac facility to comply with the strict beam requirement of proton therapy.

The beam has shown adequate stability and reproducibility to be used in meaningful radiobiology experiments even at preclinical energies. Confirming the excellent behavior demonstrated for the 35 MeV section will be the primary goal of the near future TOP-IMPLART upgrade, when multiple klystrons and modulators will be operated simultaneously and both the energy and current will be changed as fast as clinically required.

ACKNOWLEDGMENTS

This work has been funded by Innovation Department of Regione Lazio Government (Italy) Grant No. CUP: I11J10000420002.

-
- [1] <https://www.ptcog.ch/index.php/facilities-in-operation>.
- [2] R. W. Hamm, K. R. Crandall, and J. M. Potter, Preliminary design of a dedicated proton therapy linac, in *Proceedings of the 1991 Particle Accelerator Conference, San Francisco, CA, 1991* (IEEE, New York, 1991), p. 2583.
- [3] M. P. S. Nightingale, A. J. T. Holmes, and N. Griffiths, Booster linear accelerator for proton therapy, in *Proceedings of the Linear Acceleration Conference (LINAC'92), Ottawa, Ontario, Canada*, p. 398.
- [4] U. Amaldi, S. Braccini, and P. Puggioni, High frequency linacs for hadrontherapy, *Rev. Accel. Sci. Technol.* **02**, 111 (2009).
- [5] U. Amaldi, B. Szeless, M. Vretenar, E. Wilson, K. Crandall, J. Stovall, and M. Weiss, LIBO: A 3 GHz proton linac booster of 200 MeV for cancer treatment, in *Proceedings of the 19th International Linear Accelerators Conference, Chicago, IL, 1998* (NTIS, Springfield, VA, 1998), p. 633.
- [6] C. De Martinis, D. Giove, U. Amaldi, P. Berra, K. Crandall, M. Mauri, M. Weiss, R. Zennaro, E. Rosso, B. Szeless, M. Vretenar, M. R. Masullo, V. Vaccaro, L. Calabretta, and A. Rovelli, Acceleration tests of a 3 GHz proton linear accelerator (LIBO) for hadrontherapy, *Nucl. Instrum. Methods Phys. Res., Sect. A* **681**, 10 (2012).
- [7] Patent No. RM95-A000564, 1995. Inventors: L. Picardi, C. Ronsivalle, and A. Vignati; owner: ENEA.
- [8] C. Ronsivalle, M. Carpanese, C. Marino, G. Messina, L. Picardi, S. Sandri, E. Basile, B. Caccia, D. M. Castelluccio, E. Cisbani, S. Frullani, F. Ghio, V. Macellari, M. Benassi, M. D'Andrea, and L. Strigari, The TOP-IMPLART Project, *Eur. Phys. J. Plus* **126**, 1 (2011).
- [9] C. Ronsivalle, M. Carpanese, G. Messina, L. Picardi, S. Sandri, C. Marino, M. Benassi, L. Strigari, E. Cisbani, S. Frullani, and V. Macellari, The TOP-IMPLART project, in *Proceedings of the 2nd International Particle Accelerator Conference, San Sebastián, Spain* (EPS-AG, Spain, 2011), p. 3580.
- [10] S. Benedetti, A. Grudiev, and A. Latina, High gradient linacs for protontherapy, *Phys. Rev. Accel. Beams* **20**, 040101 (2017).
- [11] A. De Giovanni, P. Stabile, and D. Ungaro, LIGHT: A linear accelerator for protontherapy, in *Proceedings of NAPAC2016, Chicago, IL United States*, p. 1282.
- [12] A. De Giovanni, J. Aguilera, D. Ballestrero, S. B. Morell, A. Bonomi, R. C.-B. Magallanes, F. Caldara, M. Cerv, M. D'auria, G. De Michele, G. Dimov, V. S. Esposito, L. Esposito, M. Fanella, S. Fazio, D. A. Fink, D. Fusco, Y. Gibson, and S. C. Zannini, Status of the commissioning of the LIGHT prototype, in *Proceedings of the 9th International Particle Accelerator Conference (IPAC'18), Vancouver, British Columbia, Canada*, p. 425.
- [13] O. Losito, G. Rutigliani, L. De Palma, and F. Prudenzano, Global search methods for electromagnetic optimization of compact linac tanks, in *Proceedings of the 5th International Particle Accelerator Conference (IPAC2014), Dresden, Germany*, p. 3253.
- [14] C. Ronsivalle, L. Picardi, A. Ampollini, G. Bazzano, F. Marracino, P. Nenzi, C. Snels, V. Surrenti, M. Vadrucci, and F. Ambrosini, First acceleration of a proton beam in a side coupled drift tube linac, *Europhys. Lett.* **111**, 14002 (2015).
- [15] L. Picardi, C. Ronsivalle, and R. Hamm, Beam injection study of the TOP linac using an ACCSYS model PL-7 linac, in *Proceedings of the European Particle Accelerator Conference, Vienna, 2000* (EPS, Geneva, 2000), p. 1675.
- [16] L. Picardi, C. Ronsivalle, and S. Frullani, Progress in the development of the TOP LINAC, in *Proceedings of the XXII International Linear Acceleration Conference (LINAC2004), Lübeck, Germany*, p. 633.
- [17] L. Picardi, C. Ronsivalle, and A. Vignati, Measurements of cavities of the side coupled drift tube linac (SCDTL), in *Proceedings of the 5th European Particle Accelerator Conference (EPAC 96), Sitges, Spain*, p. 352.
- [18] L. Picardi, C. Ronsivalle, and B. Spataro, Design development of the SCDTL structure for the TOP linac, *Nucl. Instrum. Methods Phys. Res., Sect. A* **425**, 8 (1999).
- [19] L. Picardi, C. Ronsivalle, and B. Spataro, Numerical studies and measurements on the side-coupled drift tube linac (SCDTL) accelerating structure, *Nucl. Instrum. Methods Phys. Res., Sect. B* **170**, 219 (2000).
- [20] L. Picardi, C. Ronsivalle, and B. Spataro, RF behaviour of SCDTL structures, *Eur. Phys. J. Appl. Phys.* **20**, 61 (2002).
- [21] M. Ciambrella, F. Cardelli, M. Migliorati, A. Mostacci, L. Palumbo, L. Ficcadenti, V. Pettinacci, L. Picardi, and C. Ronsivalle, Electromechanical analysis of SCDTL structures, in *Proceedings of the 5th International Particle Accelerator Conference (IPAC 2014), Dresden, Germany*, p. 3250.
- [22] K. R. Crandall and M. Weiss, TERA 94/34 ACC 20, internal note, 1994.
- [23] P. Nenzi, A. Ampollini, G. Bazzano, L. Picardi, M. Piccinini, C. Ronsivalle, V. Surrenti, E. Trinca, and M. Vadrucci, Commissioning results of the TOP-IMPLART 27 MeV proton linear accelerator, in *Proceedings of the International Beam Instrumentation Conference (IBIC2016), Barcelona, Spain*, p. 686.
- [24] M. Vadrucci *et al.*, Experimental activity in the ENEA-Frascati irradiation facility with 3–7 MeV protons, in *Proceedings of the 5th International Particle Accelerator Conference (IPAC 2014), Dresden, Germany*, p. 2156.
- [25] V. Veshcherevich, An adjustable short slot hybrid for precise RF power divider system for Cornell ERL injector cavities, Technical Report No. ERL. 04–3, 2014.

- [26] P. Nenzi, A. Ampollini, G. Bazzano, L. Picardi, C. Ronsivalle, E. Trinca, V. Surrenti, and M. Vadrucci, Stability analysis of the TOP-IMPLART 35 MeV proton beam, in *Proceedings of the 9th International Particle Accelerator Conference (IPAC'18), Vancouver, British Columbia, Canada*, p. 697.
- [27] G. Bazzano, P. Nenzi, C. Ronsivalle, L. Picardi, and M. Vadrucci, Characterization of automatic frequency control systems for S-band proton linac TOP-IMPLART, in *Proceedings of the International Particle Accelerator Conference (IPAC9)*, p. 701.
- [28] E. Cisbani *et al.*, Micro pattern ionization chamber with adaptive amplifiers as dose delivery monitor for therapeutic proton linac, in *Proceedings of the International Beam Instrumentation Conference (IBIC2016), Barcelona, Spain*, p. 464.
- [29] M. Piccinini, C. Ronsivalle, A. Ampollini, G. Bazzano, L. Picardi, P. Nenzi, E. Trinca, M. Vadrucci, F. Bonfigli, E. Nichelatti, M. A. Vincenti, and R. M. Montereali, Proton beam spatial distribution and Bragg peak imaging by photoluminescence of color centers in lithium fluoride crystals at the TOP-IMPLART linear accelerator, *Nucl. Instrum. Methods Phys. Res., Sect. A* **872**, 41 (2017).
- [30] G. Baldacchini, E. De Nicola, R. M. Montereali, A. Scacco, and V. Kalinov, Optical bands of F2 and F3+ centers in LiF, *J. Phys. Chem. Solids* **61**, 21 (2000).
- [31] J. F. Ziegler, M. D. Ziegler, and J. P. Biersack, SRIM—The stopping and range of ions in matter, *Nucl. Instrum. Methods Phys. Res., Sect. B* **268**, 1818 (2010).
- [32] O. Jäkel, G. H. Hartmann, C. P. Karger, P. Heeg, and J. Rassow, Quality assurance for a treatment planning system in scanned ion beam therapy, *Med. Phys.* **27**, 1588 (2000).
- [33] S. Molinelli, A. Mairani, A. Mirandola, G. V. Freixas, T. Tessonier, S. Giordanengo, K. Parodi, M. Ciocca, and R. Orecchia, Dosimetric accuracy assessment of a treatment plan verification system for scanned proton beam radiotherapy: One-year experimental results and Monte Carlo analysis of the involved uncertainties, *Phys. Med. Biol.* **58**, 3837 (2013).
- [34] C. De Angelis, A. Ampollini, E. Basile, E. Cisbani, S. Della Monaca, F. Ghio, R. M. Montereali, L. Picardi, M. Piccinini, C. Placido, C. Ronsivalle, A. Soriani, L. Strigari, E. Trinca, and M. Vadrucci, Characterization of a 27 MeV proton beam linear accelerator, *Radiation Protection Dosimetry* **180**, 329 (2018).
- [35] C. Ronsivalle, A. Ampollini, G. Bazzano, P. Nenzi, L. Picardi, V. Surrenti, E. Trinca, and M. Vadrucci, The TOP-IMPLART linac: Machine status and experimental activity, in *Proceedings of the 8th International Particle Accelerator Conference (IPAC 2017), Copenhagen, Denmark*, p. 4669.
- [36] M. Vadrucci, A. Ampollini, F. Borgognoni, P. Nenzi, L. Picardi, C. Ronsivalle, V. Surrenti, and E. Trinca, Irradiation activity with the TOP-IMPLART proton linear accelerator, *J. Radiat. Appl.* **2**, 101 (2017).
- [37] M. Vadrucci, A. Ampollini, G. Bazzano, F. Borgognoni, P. Nenzi, L. Picardi, C. Ronsivalle, V. Surrenti, and E. Trinca, Accelerator machines and experimental activities in the ENEA Frascati particle accelerators and medical applications laboratory, in *Proceedings of the 9th International Particle Accelerator Conference (IPAC'18), Vancouver, British Columbia, Canada*, p. 460.
- [38] C. De Angelis *et al.*, The TOP-IMPLART proton linear accelerator: Characterization of the 35 MeV beam, *Radiation Protection Dosimetry* ncz142 (2019).